

Article

# Seasonal and Interannual Variations in China's Groundwater Based on GRACE Data and Multisource Hydrological Models

Jianxin Zhang <sup>1,2,3</sup>, Kai Liu <sup>1,2,3,\*</sup>  and Ming Wang <sup>1,2,3</sup>

<sup>1</sup> State Key Laboratory of Earth Surface Processes and Resource Ecology, Beijing Normal University, Beijing 100875, China; jianxinzhang@mail.bnu.edu.cn (J.Z.); wangming@bnu.edu.cn (M.W.)

<sup>2</sup> Key Laboratory of Environmental Change and Natural Disaster, Beijing Normal University, Beijing 100875, China

<sup>3</sup> Academy of Disaster Reduction and Emergency Management, Faculty of Geographical Science, Beijing 100875, China

\* Correspondence: liukai@bnu.edu.cn

Received: 3 February 2020; Accepted: 3 March 2020; Published: 5 March 2020



**Abstract:** In this study, we used *in situ* measurements for the first time to analyze the applicability and effectiveness of evaluating groundwater storage (GWS) changes across China using Gravity Recovery and Climate Experiment (GRACE) satellite products and hydrological data derived from the WaterGap Global Hydrological Model (WGHM), Global Land Data Assimilation System (GLDAS) and earth2Observe (E2O). The results show that the GWS derived from GRACE JPL Mascons products combined with GLDAS Noah V2.1 data most accurately reflect the overall distribution of GWS changes in China and the correlation coefficient between the *in situ* measurements reaches 0.538. The empirical orthogonal function decomposition for GWS indicates clear interannual variation and seasonal variation in China. The trends of China's GWS changes showed a clear regional characteristic from 2003 to 2016. The GWS in the northeast, central-south, and western junction of Xinjiang-Qinghai-Tibet had increased significantly, and the North China Plain (NCP) had a severe decline. The correlation coefficient between the annual trends of precipitation and GWS was 0.57, and it reached 0.73 when four provinces (Beijing, Tianjin, Shanxi, Hebei) that are wholly or partially located in the NCP were excluded. The seasonal variability of GWS in China was obvious and the volatilities in Jiangxi, Hunan and Fujian provinces were the highest, reaching 6.39 cm, 6.33 cm and 5.20 cm, respectively. The empirical orthogonal function decomposition for GWS and precipitation over China indicated seasonal consistency with a correlation coefficient of 0.76. The awareness of areas with significant depletion and large seasonal fluctuation of GWS help adaptations to manage local GWS situation.

**Keywords:** GRACE; Hydraulic models; TRMM; groundwater change; *in situ* measurements; China

## 1. Introduction

Excessive consumption of groundwater storage (GWS) can have a serious impact on human society. GWS resources are related to global agricultural irrigation and food safety assurance [1]. Global depletion of GWS has led to rising sea levels and has also significantly affected agricultural production at regional scales in places such as India, China, and the United States. In addition, GWS exploitation is a direct cause of differential settlement of foundations [2–5], which poses great threats to the safety of infrastructures. There is, therefore, a great need to explore the GWS change and its influencing factors.

Current methods about groundwater derivation mainly rely on *in situ* measurements, hydrological models data and remote sensing-based image [6]. The hydrological model includes Land Surface

models (LSMs) and hydrological water balance models (HMs) [6]. LSMs simulate the exchange of water and energy fluxes between the earth surface and atmosphere interface, which can generate soil moisture and water storage change, but not for GWS change [7]. Representative products are NOAH [8], MOSAIC [9], Variable Infiltration Capacity (VIC) [10], Community Land Model (CLM) [11], JULES [12]. HMs are developed for global water resources assessments and hence, human water uses are considered. The typical products include WaterGAP Global Hydrological Model (WGHM) [13], WBM [14], PCR-GLOBWB [15]. As HMs need detailed hydraulic parameters, water level observations, human water uses, land use data, etc. [6,16], accurate estimation of GWS changes and their trends from HMs still remain a challenge due to the imperfect parameterization, limited knowledge in groundwater recharge or abstractions [6,17]. As for remote sensing data, the Gravity Recovery and Climate Experiment (GRACE) mission provides technology for assessing global terrestrial water storage (TWS). The greatest advantage of GRACE is its ability to sense water stored at all levels, including GWS [18]. Together with other hydrological data, GRACE has a potential power to obtain the GWS change by removing other water storage components like soil moisture, surface water, etc. [18]. It can also be used to add useful signals to improve hydrological models [19]. There are three main official GRACE Science Data Systems that continuously release monthly gravity solutions: Geoforschungs Zentrum Potsdam (GFZ), Center for Space Research at University of Texas, Austin (CSR), Jet Propulsion Laboratory (JPL) [20,21]. GFZ releases GRACE Spherical Harmonics products, and CSR and JPL release both GRACE Spherical Harmonics and Mascons data [22–24].

GRACE combined with other hydrological data has been widely used in evaluating GWS change of different local areas in China. Huang et al. [25] used GRACE Spherical Harmonics solutions provided by CSR, four LSMs from GLDAS-1 and *in situ* measurements to detect GWS depletion in the North China Plain (NCP) and demonstrated that heterogeneous GWS variations can potentially be detected by GRACE at the sub-regional scale. Feng et al. [26] used the GRACE Spherical Harmonics solutions provided by CSR and four hydrological models ((NOAH, VIC, MOSAIC and Climate Prediction Center) to evaluate the rate of GWS depletion in the NCP. Wang et al. [27] used GRACE Spherical Harmonics solutions from CSR combined with WGHM to study the GWS change in Three Gorges Reservoir (TGR) and the trend was consistent with the *in situ* TGR measurements. GWS anomaly in the West Liaohe River Basin (WLRB) was estimated using GRACE Mascons data provided by CSR, GLDAS-1 LSMs data and *in situ* measurements from 2005 to 2015, and significant GWS depletion and interannual variability were detected [28]. Shen et al. [29] used GRACE Spherical Harmonics solutions provided by CSR and *in situ* measurements to quantify GW storage change in Hai River Basin from 2003 to 2012. These studies, however, mainly focused on the GWS changes in local areas of China, such as river basins. Furthermore, most of these studies did not give the performance of model outputs. Only two research studies quantified the accuracy of the model outputs by comparing them with *in situ* measurements. The coefficient of determination ( $R^2$ ) reach 0.75 and 0.91 in two sub-regions of the NCP between GWS derived from GRACE combined with GLDAS-1 and *in situ* measurements [25]. There was also a high  $R^2$  of 0.91 between GWS derived from GRACE combined with WGHM and *in situ* measurements in TGR [27]. The applicability of different GRACE data and hydrological model products in analyzing GWS changes over the whole of China needs to be analyzed.

This paper aimed to find a suitable product that could better evaluate the groundwater change in China by comparing with *in situ* measurements and further investigate the spatiotemporal changes in China's groundwater from a comprehensive perspective. The results provide guidance for choosing the appropriate model output when investigating China's groundwater. Section 2 presents data and brings the methodology used in this study. A comparison of different GWS datasets with *in situ* measurements was given in Section 3 followed by a comprehensive analysis of groundwater change of China, including spatial patterns, interannual changes, seasonal fluctuations, as well the relationship of GWS change and precipitation. Section 4 concludes the key findings of this study and highlights challenges for future research.

## 2. Data and Methods

### 2.1. Data

#### 2.1.1. GRACE

Five GRACE data, including GRACE Spherical Harmonic from GFZ (GFZSH), JPL (JPLSH) and CSR (CSRSH), and GRACE Mascons data provided by JPL (JPLMS) and CSR (CSRMS), were used in this study. GRACE Mascons data provided by CSR (CSRMS) were obtained from [http://www2.csr.utexas.edu/grace/RL05\\_mascons.html](http://www2.csr.utexas.edu/grace/RL05_mascons.html) and the others were obtained from the GRACE Tellus website at <ftp://podaac-ftp.jpl.nasa.gov/allData/tellus/L3/mascon/RL05/JPL/CRI/netcdf/>. The data are available for the time period from 2002 through 2017. As there are a lot of values missing in 2002 and 2017, we used the monthly time series of TWS from 2003 to 2016 for further study. Few missing monthly records were interpolated using the data of neighboring months [30].

The spatial resolution of GRACE data we used were  $0.5^\circ \times 0.5^\circ$  and  $1^\circ \times 1^\circ$  for GRACE Mascons data and GRACE Spherical Harmonics data, respectively. The GRACE data were multiplied by dimensionless gain factors [22,23] and the resolution of gain factors are consistent with GRACE data (i.e., 0.5 degree for GRACE Mascons and 1 degree for GRACE Spherical Harmonics, respectively) but it doesn't need to apply any additional filtering or gain factors to CSRMS [24].

#### 2.1.2. GLDAS

GLDAS is a satellite mission that uses land surface models to estimate the global distributions of land surface states such as soil moisture, snow water equivalent, run-off, etc. [7]. The resolution of GLDAS data we used is  $1^\circ \times 1^\circ$ . In this study, the monthly time series for soil water storage (SWS), snow water equivalent (SWE), and vegetation canopy water storage (CWS) were obtained from GLDAS Noah V2.1, CLM, Mosaic, VIC, Noah V001 at (<http://disc.sci.gsfc.nasa.gov/uui/datasets?keywords=GLDAS>).

#### 2.1.3. E2O

Earth2Observe “Global Earth Observation for Integrated Water Resource Assessment” is a collaborative project funded under the Directorate-General (DG) Research Framework Programme 7 (FP7) [31]. Earth2Observe integrates available global earth observations (EOs), *in situ* datasets and models and construct a global water resources reanalysis dataset spanning a significant length of time (several decades). E2O provides not only SWS, SWE and CWS, but also additional GWS data. The spatial and temporal resolutions are  $0.25^\circ \times 0.25^\circ$  and monthly, respectively, and the units are  $\text{kg}/\text{m}^2$ . Here, the Water Resource Re-analysis v2 was used. We obtained the total canopy water storage from Meteo France at <https://wci.earth2observe.eu/portal/?state=e81f65>, the snow water equivalent from CEH at <https://wci.earth2observe.eu/portal/?state=694667>, the total moisture from ECMWF at <https://wci.earth2observe.eu/portal/?state=3a881f>, and the GWS from Australian National University on <https://wci.earth2observe.eu/portal/?state=130a65>.

#### 2.1.4. WGHM

The WaterGAP Global Hydrological Model (WGHM) was developed by Döll et al. [32]. It is a submodel of the global water use and availability model WaterGAP 2, and it computes surface runoff, groundwater recharge and river discharge at a spatial resolution of  $0.5^\circ \times 0.5^\circ$  and is able to calculate reliable and meaningful indicators of water availability at a high spatial resolution of  $0.5^\circ \times 0.5^\circ$  [32]. The data are available on [http://www.uni-frankfurt.de/49903932/7\\_GWdepletion](http://www.uni-frankfurt.de/49903932/7_GWdepletion). The monthly time series of GWS from WaterGAP for the period of 2005-2013 were used.

#### 2.1.5. *In Situ* Measurements

We obtained groundwater level (GWL) observations from the “China Geological Environment Monitoring groundwater Level Yearbook” [33] for groundwater wells provided by the Ministry of

Water Resources of China for the period of 2005–2013. The GWL is expressed in terms of depth based on the 1956 Yellow Sea elevation system, and the unit is “meter”. The total number of observation wells is 892 and due to the discontinuous observation records in most wells, we only kept 315 wells with continuous time series for analysis.

The groundwater level change from *in situ* measurements was obtained by using the elevation of monitoring wells to minus the mean of monthly burial depth. To compare the results from the observation wells with the GRACE-derived GWS data, the groundwater levels obtained from the wells for a given year were subtracted from the average groundwater levels from 2005 to 2009.

#### 2.1.6. TRMM

The TRMM Multisatellite Precipitation Analysis (TMPA) was designed to combine all available precipitation datasets from different satellite sensors and monthly surface rain gauge data to provide an estimate of precipitation at a spatial resolution of  $0.25^\circ \times 0.25^\circ$  for the areas between  $50^\circ\text{N}$  and  $50^\circ\text{S}$  [34]. TRMM 3B43, which provides monthly data, is used in this study. The data are available at <https://pmm.nasa.gov/data-access/downloads/trmm>.

### 2.2. Methods

#### 2.2.1. Deriving GWS

The vertical water balance model generally suggests that **terrestrial water storage (TWS) = soil water storage (SWS) + surface water storage** (including snow water equivalent (SWE), vegetation canopy water content (CWS), rivers, lakes, reservoirs storage) + **groundwater storage (GWS)** [35,36]. Due to the fact that the accurate data of lakes, rivers, reservoirs data for whole China are unavailable, we ignored them in this study and GWS can be calculated according to Equation (1):

$$GWS = TWS - (SWS + SWE + CWS) \quad (1)$$

In this study, we obtained TWS from GRACE and SWS, SWE and CWS from GLDAS and E2O data. Four approaches were used: (1) GWS derived from GRACE combined with GLDAS. There are 5 products for GRACE and GLDAS, respectively, resulting a total of 25 combinations; (2) GWS provided by E2O; (3) GWS derived from GRACE combined with E2O and there are 5 combinations; (4) GWS provided by WGHM. To be consistent with the GRACE data, SWS, SWE and CWS from GLDAS and E2O for a given year were computed to obtain an anomaly relative to the same baseline time period with GRACE (2004–2009). GRACE Mascons Data with a resolution of 0.5 degree was upscaled to 1 degree using the average of four nearest grids, while the SWS, SWE and CWS derived from E2O with a resolution of 0.25 degree were upscaled to 1 degree using the average of sixteen nearest grids.

#### 2.2.2. Median Trend Analysis and Mann-Kendall Test

The nonparametric Mann–Kendall trend test with Sen’s slope estimator was used to identify the GWS trend. The Theil–Sen median trend analysis is a robust trend statistical method [37], and it calculates the median slopes between all  $n(n-1)/2$  pairwise combinations of the time series data [38]. The Theil–Sen median trend  $T$  is calculated by Equation (2):

$$T = \text{median}\left(\frac{W_j - W_i}{j - i}\right) \quad (2)$$

where  $i$  and  $j$  represent different time units (months or years; in this paper, they refer to years),  $W_j$  and  $W_i$  represent data for different years. The purpose of the Mann–Kendall (MK) test [39–41] is to statistically assess if there is a monotonic upward or downward trend of the variable of interest over time. We evaluated the statistical significance of the GWS and precipitation trends and determined the linear slopes for trends using the Mann–Kendall nonparametric test, as shown in Asoka et al. [42].

### 2.2.3. The Empirical Orthogonal Function (EOF) Decomposition

The empirical orthogonal function (EOF), also known as the eigenvector analysis or principal component analysis (PCA), is a method of analyzing structural features in matrix data and extracting the amount of primary data features, including times series and spatial patterns. Lorenz [43] first introduced it to meteorological and climatic research in the 1950s and it is now widely used in the geosciences, hydrology and other disciplines [42,44–48].

### 2.2.4. Three-Cornered Hat Method

Three-Cornered Hat Method (TCH) was used to estimate the relative uncertainties of GWS derived from different GRACE and hydrological models data [49–52]. Considering the time series of the available GWS products  $\{X_i\}_{i=1,2,\dots,N}$ , where  $i$  corresponds to each GWS product, let each time series be expressed by Equation (3):

$$X_i = S + \varepsilon_i \quad \forall i = 1, 2, \dots, N \quad (3)$$

where  $S$  is the true signal and  $\varepsilon_i$  represents the measurement error [53]. Due to no true estimate of  $S$  being available, the  $N-1$  GWS products and one designed as the reference (chosen arbitrarily) could be computed by Equation (4) [54]:

$$Y_{iN} = X_i - X_N = \varepsilon_i - \varepsilon_N \quad \forall i = 1, 2, \dots, N \quad (4)$$

where  $X_N$  is the reference time series. The results are independent of the special choice of a GWS product [50,54]. Then covariance matrix  $S$  of the series of difference is computed. Introducing the unknown  $N \times N$  covariance matrix of individual noises  $\begin{bmatrix} \widehat{R} & r \\ r^T & r_{NN} \end{bmatrix}$ , it is related to  $S$  by Galindo and Palacio and we have the Equation (5) [55]:

$$S = [I - u] \bullet \begin{bmatrix} \widehat{R} & r \\ r^T & r_{NN} \end{bmatrix} \bullet \begin{bmatrix} I \\ -u^T \end{bmatrix} \quad (5)$$

where  $I$  is the  $(N-1) \times (N-1)$  identity matrix,  $r$  refers the  $(N-1)$  vector  $[r_{1N} \ r_{2N} \ \dots \ r_{N-1,N}]^T$ ,  $u$  is the  $(N-1)$  vector  $[1 \ 1 \ \dots \ 1]^T$ .  $\widehat{R}$  can be computed by Equation (6):

$$\widehat{R} = S - r_{NN}[uu^T] + ur^T + ru^T \quad (6)$$

Equation (5) is undetermined. To determine the  $N$  free parameters, a suitable objective function should be defined. The suggested objective function is given by Galindo and Palacio as shown in Equation (7) [52]:

$$F(r_{1N}, \dots, r_{NN}) = \sum_{i < j}^N \frac{r_{ij}^2}{K^2} \quad (7)$$

with a constraint function shown Equation (8):

$$G(r, r_{NN}) = -\frac{r_{NN} - [r - r_{NN}u]^T \cdot S^{-1} \cdot [r - r_{NN}u]}{K} < 0 \quad (8)$$

where  $K$  denotes  $K = \sqrt[n]{\det(S)}$ . The initial conditions are selected to assure that the initial values fulfilled the constrains and it is shown in Equation (9) [51]:

$$r_{iN}^{(0)} = 0, \quad i < N \quad \text{and} \quad r_{NN}^{(0)} = (2 \cdot u^T \cdot S^{-1} \cdot u)^{-1} \quad (9)$$

After determining the free parameters ( $r_{1N}, r_{2N}, \dots, r_{NN}$ ) by minimizing Equation (7), the remaining unknown elements can be computed using Equation (6) and the square root of diagonal elements of  $\widehat{R}$  and the  $r_{NN}$  represent the uncertainties between different datasets.

### 3. Results

#### 3.1. Comparison of Different GWS Data Sets

The Sen's slopes of the derived GWS from the different datasets from 2005 to 2013 were calculated for China (Figure 1). The time period from 2005 to 2013 was selected because the observation wells data were only available for this time period. Since there are 30 combinations of derived GWS from GRACE combined with GLDAS and E2O, here, we only present the two best results, i.e., JPLMS combined with GLDAS Noah V2.1 and JPLMS combined with E2O according to the comparison with the *in situ* measurements that follow. The results of the complete datasets can be referred to Figure S1 in the Supplementary file. The results show that the annual trends of GWS derived from GRACE JPLMS combined with E2O (Figure 1b) and GRACE JPLMS combined with GLDAS Noah V2.1 (Figure 1c) shows similar spatial patterns—an increasing trend in southern China and a significant decrease in the NCP. GWS derived from E2O (Figure 1a) shows quite different patterns where a particularly clear increase in GWS in northeastern China and a decline in Tibet Plateau were observed, while the GWS derived from WGHM (Figure 1d) shows increasing trends in most parts of China and a severe decline in the NCP.

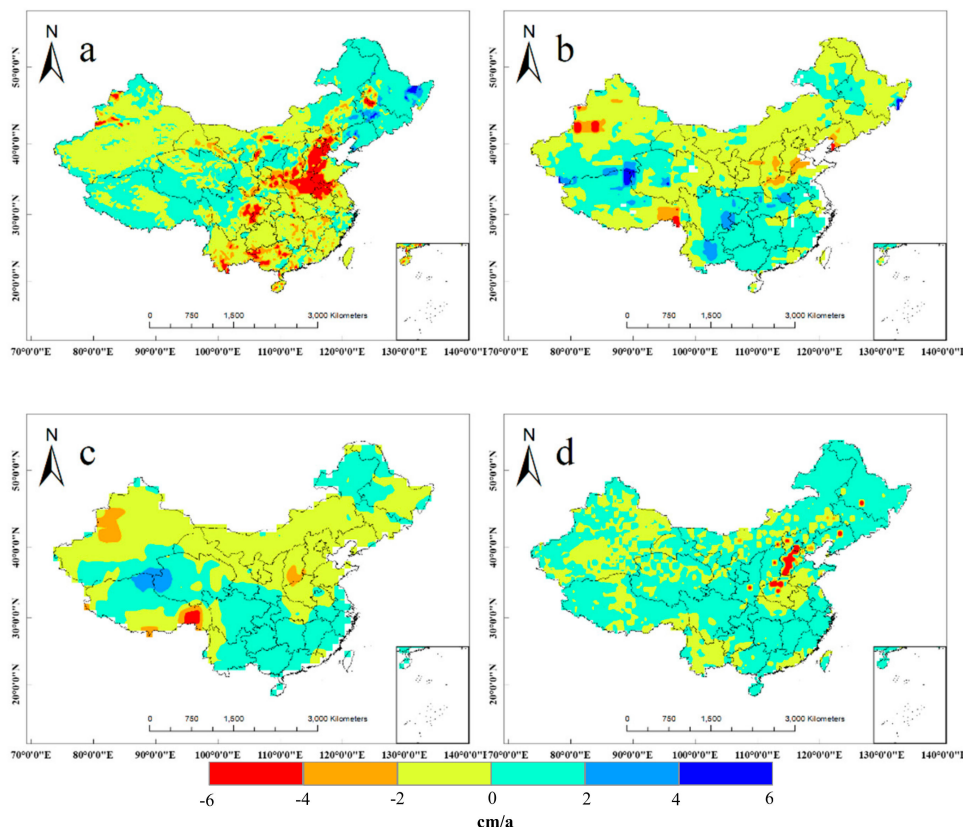


**Figure 1.** The interannual trend of GWS derived from different data sets during the period 2005–2013, including: (a) GWS derived from E2O, (b) GWS derived from GRACE JPLMS combined with E2O, (c) GWS derived from GRACE JPLMS combined with GLDAS Noah V2.1, (d) GWS derived from WGHM.

Figure 2 gives the uncertainties of the GWS derived from different datasets computed from the TCH method given in Section 2.2.4. We can see that the GWS derived from GRACE JPLMS combined

with E2O (Figure 2b) and GWS derived from GRACE JPLMS combined with GLADAS Noah V2.1 (Figure 2c) have relatively low uncertainties, with national average uncertainties of 3.7 cm and 2.28 cm, respectively. The GWS derived from WGHM exhibits the largest uncertainties with a national average uncertainty of 13.1 cm, and the largest uncertainties were observed in southern China and the NCP.

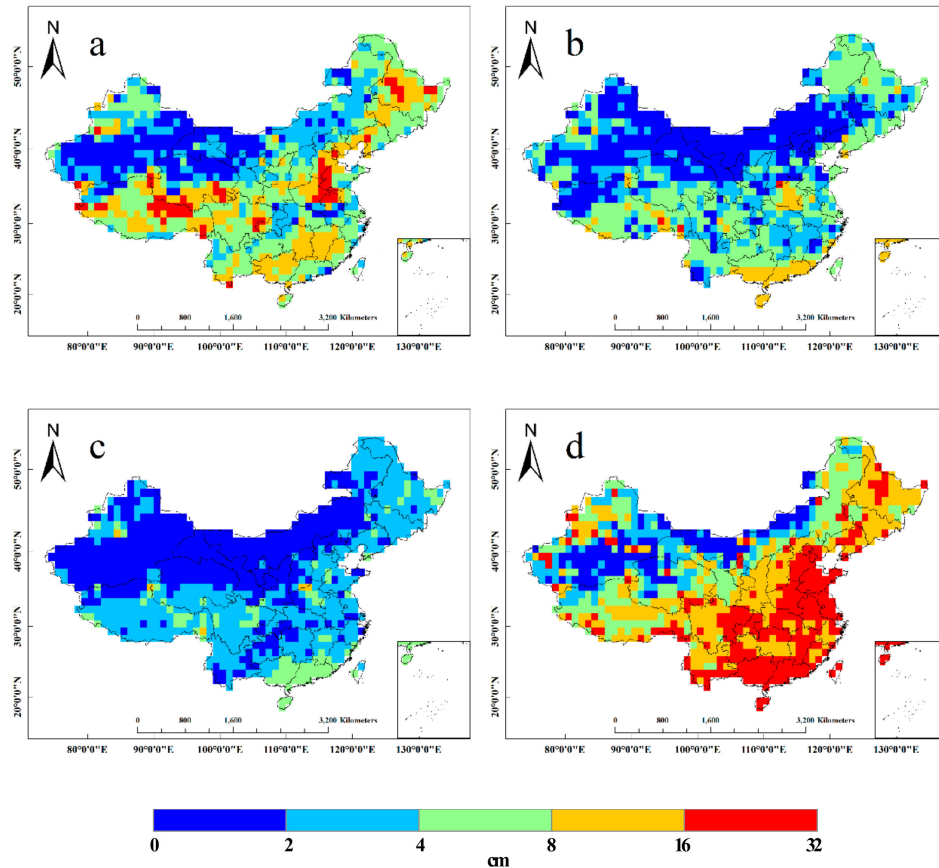


**Figure 2.** Uncertainties of the GWS, including (a) GWS derived from E2O, (b) GWS derived from GRACE JPLMS combined with E2O, (c) GWS derived from GRACE JPLMS combined with GLADAS Noah V2.1, (d) GWS derived from WGHM.

We further compared the changes in GWS from the four approaches presented above with changes in groundwater levels change from observation wells. Figure 3 presents the spatial temporal trend of GWS based on recorded data from observation wells with statistical significance at the 5% level under the conditions of the MK test ( $p < 0.05$ ). In general, there is an increasing trend in GWS in southern China and a decreasing trend in northern China.

Figure 4 shows that the correlation coefficients between the annual trend derived from *in situ* measurements and GRACE JPLMS combined with hydraulic models, and the annual trends of observation wells in the same grid were averaged. Two limitations of this comparison have to be addressed, i.e., (1) there is a spatial mismatch between the global resolution data and point scale measurements; (2) the *in situ* measurements measure the groundwater level change instead of ground water storage change. Nevertheless, this comparison measures how strong a relationship is between the two from a general perspective. From Figure 3, we can see that the derived GWS range from 0.066 to 0.538 ( $p < 0.05$ ). The GWS derived from GRACE JPLMS and GLDAS Noah V2.1 have the best correlation with the observed data, while the GWS derived from WGHM have the worst correlation. The results imply that the GRACE JPL Mascons products combined with the GLDAS Noah V2.1 data was a relatively reasonable and reliable dataset to represent GWS changes in China. This dataset

was therefore adopted for further analysis and the time period of the GWS data was extended from 2005–2013 to 2003–2016.

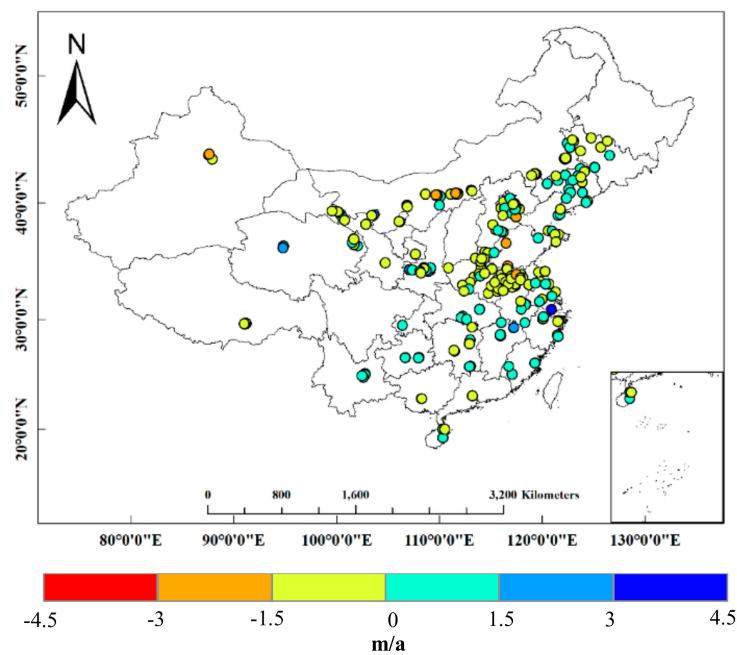


Figure 3. Spatial distribution of *in situ* measurements and the annual trend from 2005 to 2013.

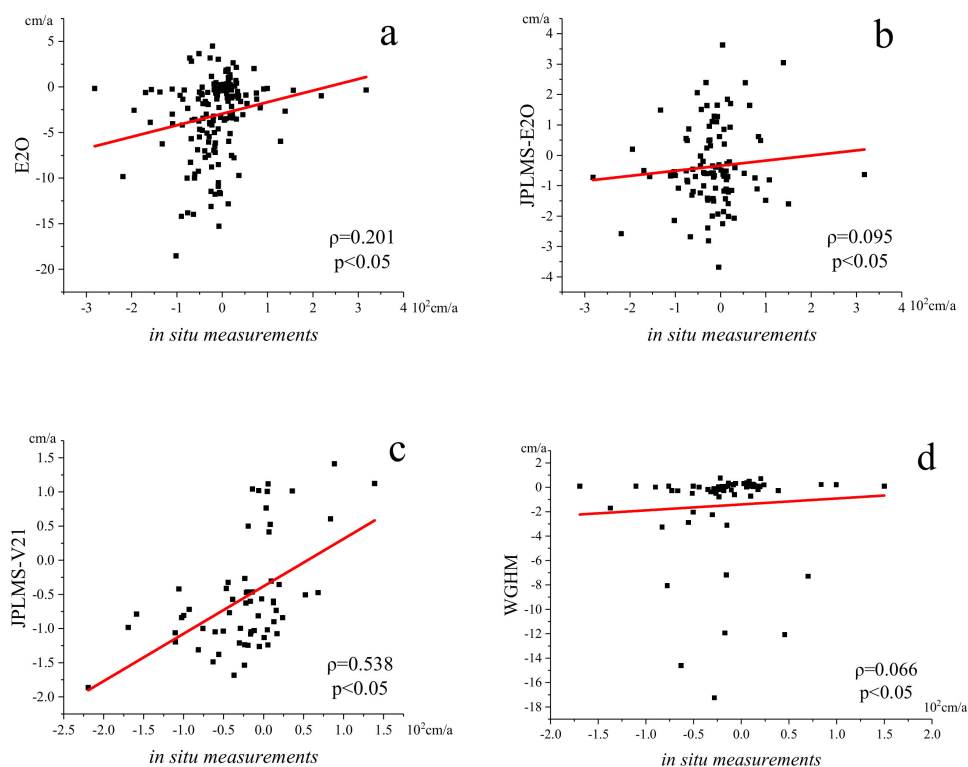
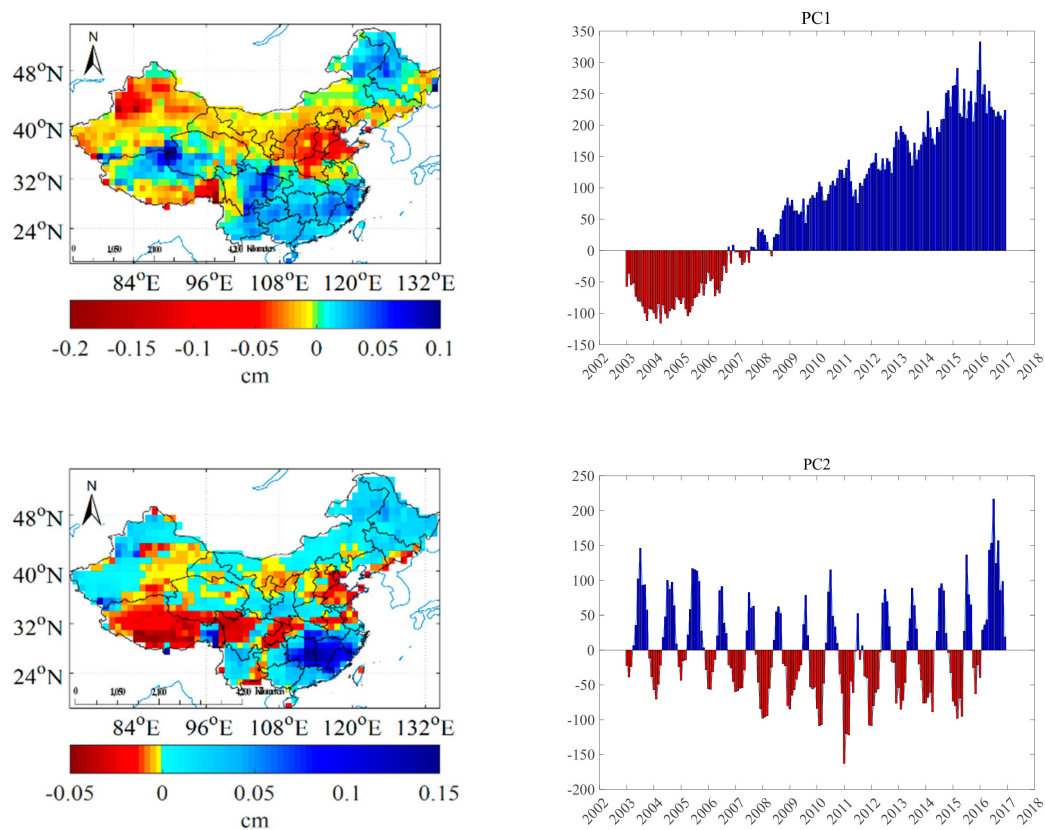


Figure 4. Scatter diagrams between *in situ* measurements and GWS derived from different datasets. The correlations were computed with statistical significance at the 5% level. (a) *in situ* measurements and GWS derived from E2O; (b) *in situ* measurements and GWS derived from GRACE JPLMS combined with E2O; (c) *in situ* measurements and GWS derived from GRACE JPLMS combined with GLDAS Noah V2.1; (d) *in situ* measurements and GWS derived from WGHM). Trends were estimated using the nonparametric Mann–Kendall test and Sen’s slope method.

### 3.2. EOF Analysis of GWS Changes in China

We decomposed the monthly GWS time series from 2003 to 2016 using the EOF method. Figure 5 shows the spatial patterns (EOF model 1 and mode 2) of the GWS changes and the associated principle components (PC1 and PC2). The long-term trends and seasonal variability were captured by the first two modes of the EOF analysis, which explain 52.61% and 13.19% of the total variance, respectively.



**Figure 5.** Spatial patterns of GWS anomaly for EOF modes 1 and 2 during the period Jan. 2003–Dec. 2016 (left panels) and the amplitude time series (principal components) for modes 1 and 2 (right panels).

PC1 is associated with the long-term trends and interannual variability of GWS. A climatological shift occurred in August between 2007 and 2008. The spatial pattern of mode 1 shows positive GWS deviations in southeast China, the Qinghai-Tibet Plateau, and the Heilongjiang River Basin but negative deviations in most part of North China, especially Tien Shan region in northwestern China's Xinjiang Province, southern Tibet, and the NCP. Combined with amplitude time series PC1, the results show that the GWS changes in southeast China, the Qinghai-Tibet Plateau, and the Heilongjiang River Basin decreased during 2003–2007 and increased during 2008–2016, while other regions had the opposite pattern, indicating that they experienced GWS decrease after 2008.

PC2 is associated with the dominant seasonal features. The amplitude of PC2 approximates a sine wave with peaks in May - September and troughs in December - March. Combined with the spatial pattern of mode 2, we can see an increasing trend for the GWS change between May and September and a decreasing trend between December and March in southeast China, northeastern China (Heilongjiang, Jilin, and Liaoning provinces and the Inner Mongolia Autonomous Region), and the northwestern part of Xinjiang.

It is known that precipitation plays an important role in replenishing the GWS. In the next section, we quantify how GWS is influenced by precipitation variability throughout China.

### 3.3. Interannual Variation in GWS

The interannual trends of GWS during 2003–2016 were calculated and are shown in Figure 6a. The results show clear regional characteristics of GWS changes. In southern China, including Sichuan, Chongqing, Hubei, Anhui, and Jiangsu provinces, there were clear increasing trends. Increasing trends were also observed in most of the Qinghai-Tibet region (except the southeast corner), the northeastern Inner Mongolia Autonomous Region and Heilongjiang Province. Significant declines in GWS were observed in the Tien Shan region in northwest of China's Xinjiang Province, southeastern Tibet, and the NCP. The largest decrease was  $-7.98$  cm/a in southeastern Tibet.

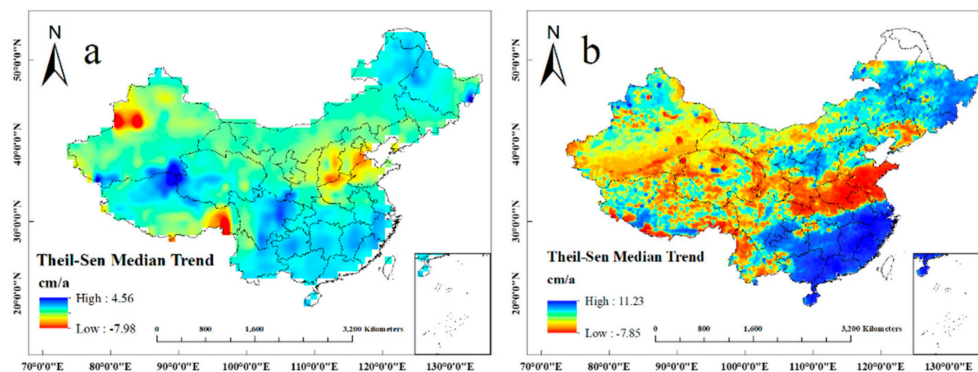


**Figure 6.** (a) Interannual trends of GWS change and (b) precipitation (in cm/a) during 2003–2016.

We analyzed the correlation between precipitation and GWS at the provincial level. Figure 6 shows the trends of annual precipitation and GWS in China during 2003–2016. The results show significant increases in precipitation in southeastern and northeastern China, which correspond to increases in GWS in the corresponding regions, while most regions of Northern China show decreasing trends in precipitation which is also highly consistent with the decreasing trend of GWS. However, inconsistency exists between the two. For example, an apparent GWS decrease was found in the east of Himalaya Mountains, northern Tarim Basin but not for the precipitation. Due to the fact that the glacier mass change was not excluded from GRACE [56], the decrease was mainly caused by glacier mass change rather than GWS depletion [57–61]. The GWS showed a clear increase in Qinghai-Tibet while there was a decrease in precipitation. Although the precipitation in this region shows a declining trend from 2003 to 2016, the average precipitation was  $242.99$  mm yr<sup>-1</sup>, larger than the 1998–2002 average of  $224.31$  mm yr<sup>-1</sup>. The increasing trend of GWS is mainly due to the replenishment of GWS after a prolonged dry period from 1998–2002 [61]. We also found that despite increases in precipitation in Beijing, Tianjin, Hebei, and Shanxi, which are partially or wholly in the NCP, there was a severe decrease in GWS.

We further calculated the correlation coefficients between the trend of GWS and precipitation at the provincial level (Figure 7). There is a relatively high correlation of 0.573 between the interannual variations in the TRMM data and the GWS. The correlation between the two would reach 0.73 when four provinces (Beijing, Tianjin, Hebei, and Shanxi) which are mainly in or around the NCP were excluded. It is well known that the groundwater depletion is seriously affected by the anthropogenic factors in the NCP [1,26,61]. Figure 8 shows the ratio of average irrigated area of cultivated land at provincial level from 2003–2016 and the GWS consumption was the largest in the NCP and the pattern was highly consistent with GWS depletion depicted in Figure 5a. The NCP is the premier irrigated area in China and the Plain has 17,950 thousand ha of cultivated land, about 71.7 percent of which is irrigated and the crop production largely relies on underground water [62,63]. The increase of coefficient between GWS and TRMM when four provinces (Beijing, Tianjin, Hebei, and Shanxi) were excluded also proves the influence of human factors in the NCP.

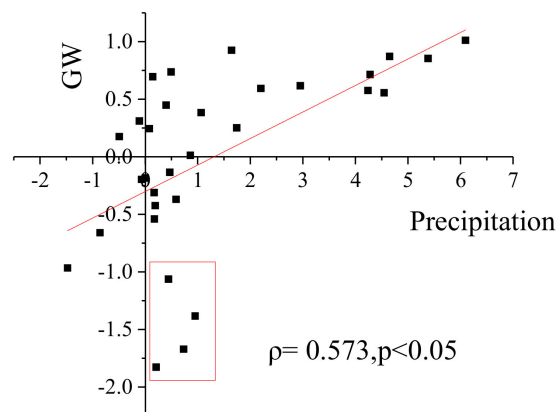


**Figure 7.** Scatter plot showing the interannual trend between TRMM data and GWS in China at the provincial level. The points in the red rectangle refer to Beijing, Tianjin, Hebei and Shanxi provinces, which are mainly in or around the NCP.

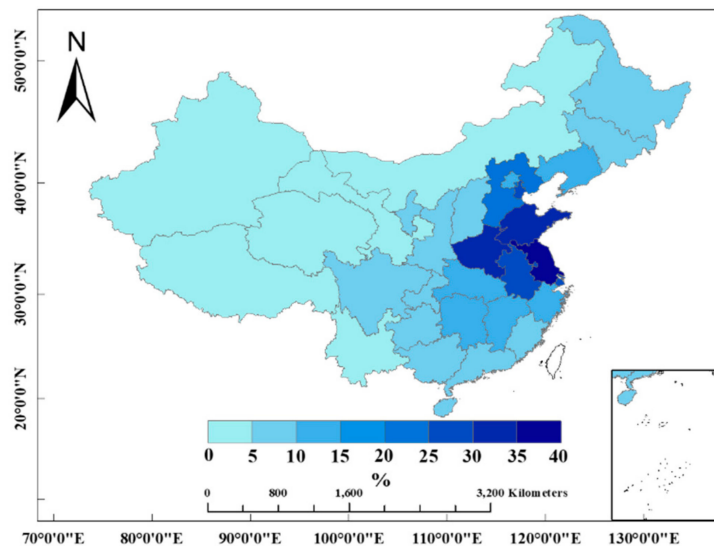


**Figure 8.** The ratio of average irrigated area of cultivated land at provincial level from 2003 to 2016 in China.

### 3.4. Seasonal Variation in GWS

In addition to the interannual variation, we also investigated the GWS fluctuations during the year. Fluctuations in GWS may lead to ground settlement, which can pose great risks to infrastructure [2].

Figure 9 shows the fluctuations in the time series of GWS and precipitation from 2003 to 2016. The peaks and troughs are highly consistent, and the correlation coefficient is 0.52. These results show that GWS changes are substantially affected by rainfall throughout China. We then decomposed precipitation from the TRMM data using the EOF method to determine the seasonal variation. Detrend of the anomalies derived from precipitation was performed. As shown in Figure 10, the amplitude of PC1, which explains 53.59% of the total precipitation variability, shows similar seasonal cycles as GWS. Troughs exist from January to April and from October to December, and peaks are observed from May to September. This indicates that the amplitude time series of mode 1 captures the 5-month phase shift of the monsoon season (May - September). A comparison of PC2 of GWS and PC1 of precipitation shows that the seasonal variation in GWS is highly consistent with the seasonal variation in precipitation, indicating that precipitation plays an important role in GWS changes. The correlation coefficient is 0.76 and this indicates that the seasonal change in precipitation can be a reliable indicator of the seasonal change in GWS.

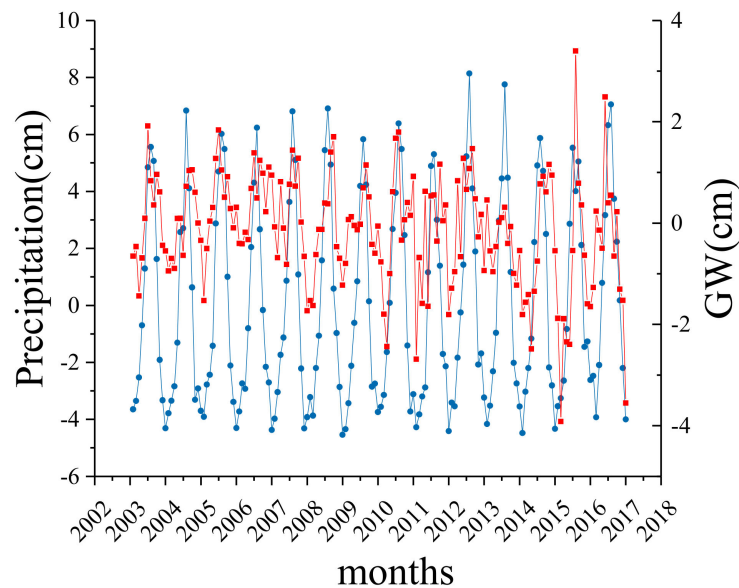


**Figure 9.** Mean monthly fluctuations between GWS derived from JPLMS combined with GLDAS Noah V2.1 and precipitation anomalies over China during Jan. 2003–Dec. 2016. The blue lines represent the precipitation anomaly, and the red lines indicate the GWS changes. The time lag between GWS and precipitation was 1 month.

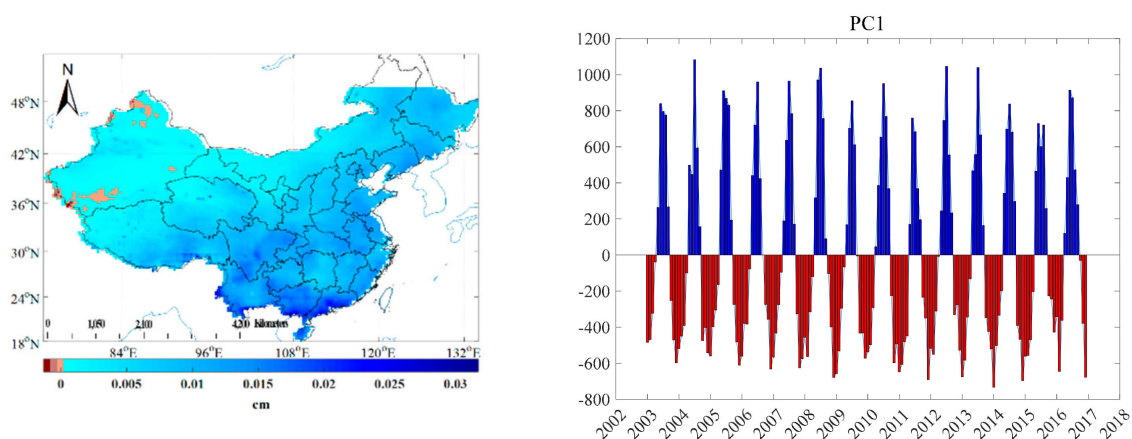


**Figure 10.** Spatial patterns of precipitation anomaly for EOF mode 1 during the period Jan. 2003–Dec. 2016 (left panel) and the amplitude time series (principal components) for mode 1 (right panel).

To further investigate the relationship between precipitation and GWS, we computed the seasonal fluctuation of main river basins [64]: Songhua and Liaohe River Basin (SLRB), Continental Basin (CB), Haihe River Basin (HRB), Huaihe River Basin (HHRB), Southwest Basin (SWB), Southeast Basin (SEB), Yangtze River Basin (YZRB), Pearl River Basin (PRB), Yellow River Basin (YRB) (Figure 11). Figure 12 shows the calculated correlation coefficients between the GWS and precipitation for 9 river basins at a maximum time lag of 48 months. We can see that correlations are significant ( $\rho > 0.4$ ) in 7 of the 9 river basins. The maximum correlation ( $\rho = 0.63$ ) was observed in Yangtze River Basin with a time lag of 1 month. Haihe River Basin ( $\rho = 0.27$  at 17 months) and Huaihe River Basin ( $\rho = 0.23$  at 9 months) showed the lowest correlations and responded at long time scales. These two basins are located in the NCP and the results highlight the effect of human activities on the GWS response to precipitation.

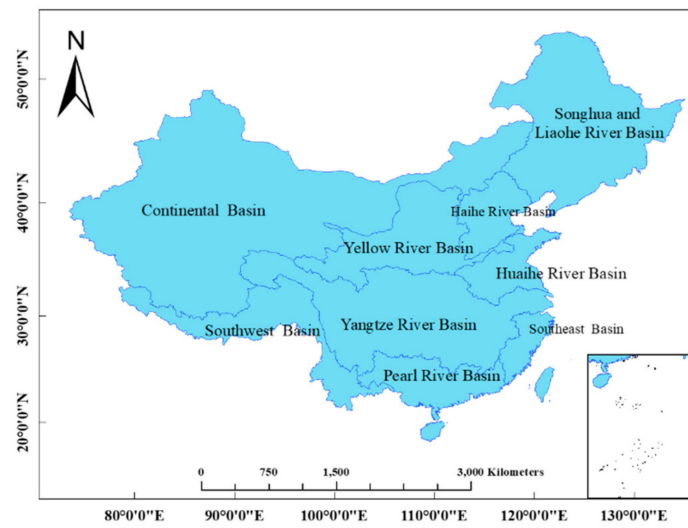


Figure 11. Main river basins in China.

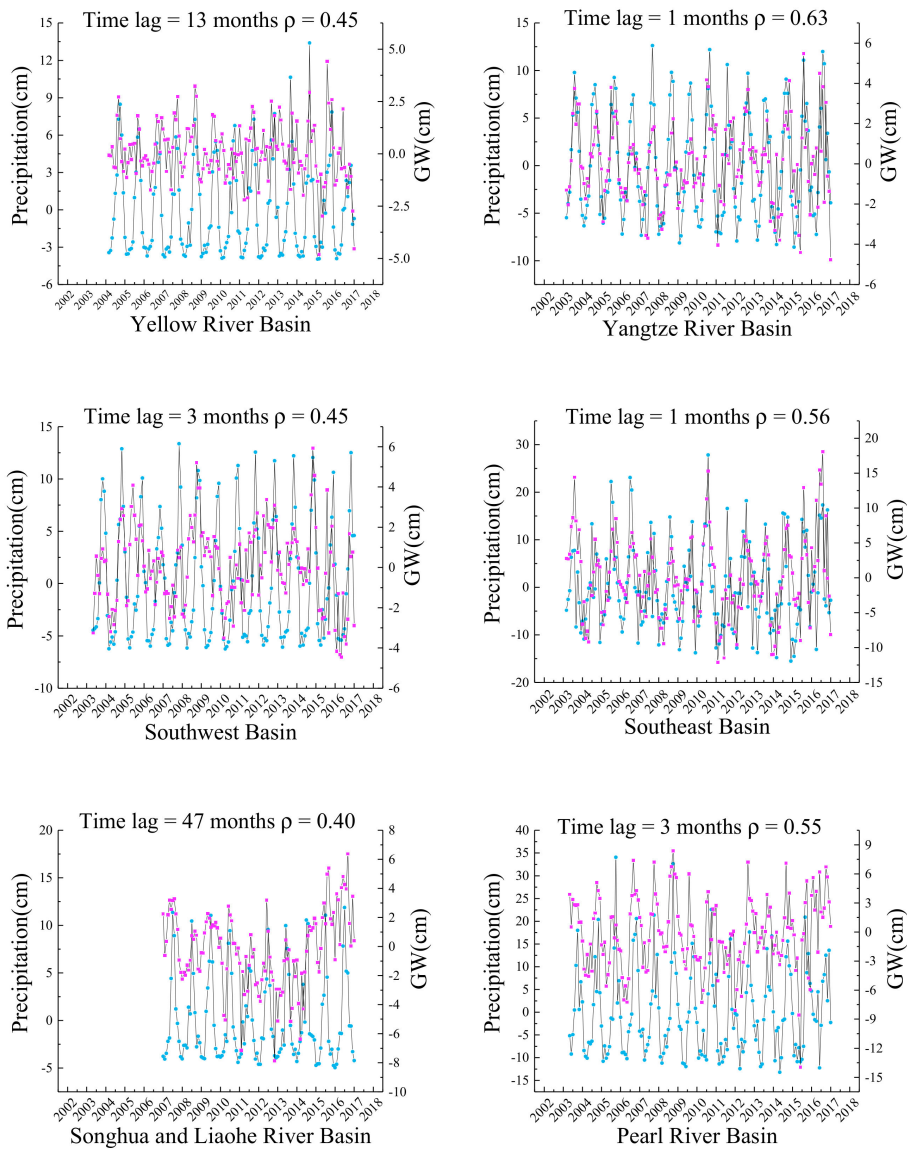
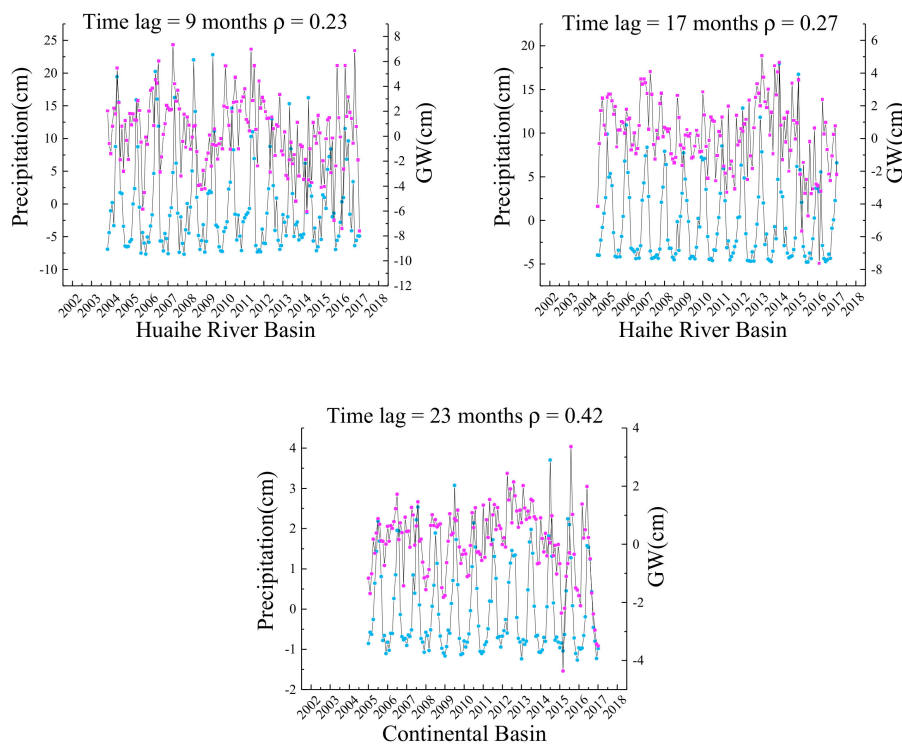
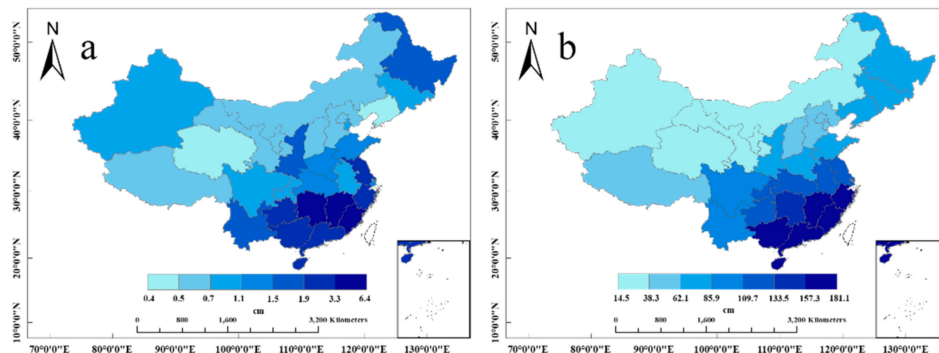


Figure 12. Cont.



**Figure 12.** Maximum Pearson’s Correlation Coefficient  $\rho$  between GWS and precipitation in different river basins during Jan. 2003–Dec. 2016 at maximum time lag of 48 months. The blue and purple lines represent the precipitation anomalies and GWS changes, respectively.

The fluctuation in GWS at the provincial level was quantified. We calculated the standard deviation of annual GWS derived from monthly climatological means in GWS change based on data from 2003–2016. The results show that the greatest fluctuation of GWS is in Jiangxi province and the standard deviation is 6.39 cm. Hunan and Fujian provinces also have large fluctuations of 6.33 cm and 5.20 cm, respectively. Generally, the fluctuation in GWS is fairly consistent with the annual precipitation (Figure 13): higher fluctuations of GWS occur in areas with higher annual precipitation, except for Xinjiang Province, where a relatively large fluctuation of GWS and low annual precipitation are observed. To quantify the correlation between precipitation and GWS fluctuation, we compared the ranking of provinces by seasonal fluctuations of GWS change and annual precipitation. The result is shown in Figure 14. It can be seen that there is a high consistency between the two and the correlation reaches 0.74. The top seven provinces with the highest groundwater fluctuations are exactly the same as the top seven provinces with the highest annual precipitation, which are Jiangxi, Hunan, Fujian, Guangxi, Zhejiang, Guangdong, and Hainan.



**Figure 13.** Seasonal fluctuations of GWS change (a) and annual precipitation at the provincial level (b) from 2003 to 2016.

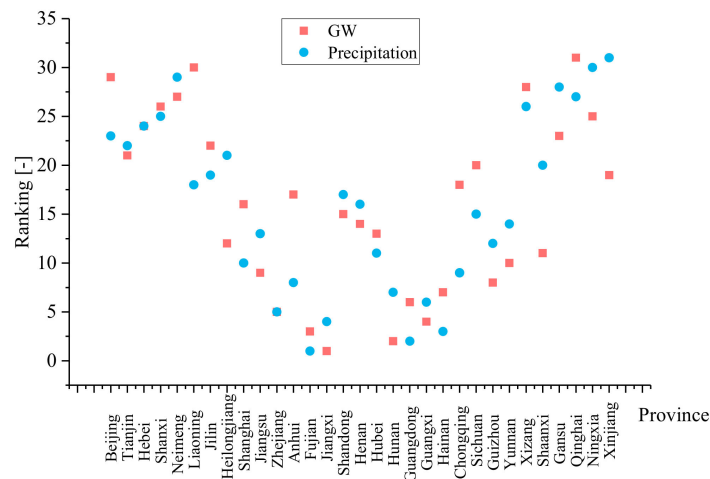


**Figure 14.** The ranking of seasonal fluctuations of GWS and annual precipitation at the provincial level.

#### 4. Conclusions

We compared GWS values derived from different combinations of GRACE and hydrological models data with *in situ* measurements at a national scale of China for the first time. The results indicate that GWS derived from JPLMS combined with GLDAS Noah V2.1 outperforms to reflect the spatiotemporal variations throughout China shown by the *in situ* observations, which provides guidance for choosing an appropriate method to derive the GWS of China.

A comprehensive analysis of GWS change in China was analyzed, including spatial patterns, interannual changes, seasonal fluctuations, etc. China's GWS changes show clear interannual trends and seasonal variations during the period of 2003–2016. The change rate of regional GWS in China varied spatially, which was mainly reflected in generally increasing trends in the south-central region, the junction between Heilongjiang and Inner Mongolia and Xinjiang–Qinghai–Tibet boundaries. Significant declines in GWS were observed in the Tien Shan region in northwest of China's Xinjiang Province, southern Tibet, and the NCP. The largest decrease was  $-7.98$  cm/a in the southeastern Tibet. The interannual trends of GWS in most regions were consistent with those of precipitation but not in part of the NCP. Social and human factors could be significant drivers of the decreasing trend of GWS in the NCP.

The seasonal fluctuations of GWS in China were consistent with the precipitation. China's precipitation showed peaks during May–September, and the peaks period of precipitation override the peaks of GWS. A low correlation was observed for Haihe River Basin ( $\rho = 0.27$  at 17 months) and Huaihe River Basin ( $\rho = 0.23$  at 9 months) which are located in the NCP, which also highlights the effect of human activities on the GWS response to precipitation. Provinces with large GWS fluctuations are identified. The awareness of areas with significant depletion and large seasonal variation of GWS help adaptations to cope with local GWS situation.

We have to admit that the method used in this study to derive GWS is imperfect and uncertainties exist. Recently, data assimilation techniques have been proposed to improve the simulation of hydrological models by assimilating the GRACE observation into hydraulic models [65–69]. We will use these new techniques in our future studies to enhance the accuracy of the GWS estimate. Meanwhile, further studies will be performed to quantify the contribution of natural and human-induced processes on the GWS of China at a provincial scale and hydrological settings.

**Supplementary Materials:** The following are available online at <http://www.mdpi.com/2072-4292/12/5/845/s1>.

**Author Contributions:** Conceptualization, K.L.; Methodology, J.Z., K.L., and M.W.; Validation, J.Z. and K.L.; Formal Analysis, J.Z. and K.L.; Investigation, J.Z., K.L., and M.W.; Resources, J.Z. and K.L.; Data Curation, J.Z. and K.L.; Writing-Original Draft Preparation, J.Z.; Writing-Review & Editing, K.L.; Visualization, and K.L.; Supervision, K.L.; Project Administration, K.L.; Funding Acquisition, K.L. All authors have read and agreed to the published version of the manuscript.

**Funding:** This research was funded by National Natural Science Foundation of China (41771538) and National Key Research and Development Plan (2017YFC1502901).

**Acknowledgments:** The research for this article was supported by the National Natural Science Foundation of China (41771538) and National Key Research and Development Plan (2017YFC1502901). The financial support is highly appreciated. There is no conflict of interest to declare. We appreciate Petra Döll with the Institute of Physical Geography, Goethe University Frankfurt, Germany, for her providing the WGHM output. We would like to thank GRACE Mascon data supported by the NASA MEaSUREs Program, GLDAS Noah V2.1 from the Goddard Earth Sciences Data and Information Services Center, NASA and Earth2Observe for providing E2O outputs. We would like to thank The TRMM 3B43 data were provided by the NASA/Goddard Space Flight Center's and PPS, which develop and compute the TMPA data as a contribution to TRMM and archived at the NASA GES DISC. Sincere acknowledgement for the data support from "Geographic Data Sharing Infrastructure, College of Urban and Environmental Science, Peking University".

**Conflicts of Interest:** The authors declare no conflicts of interest.

## References

1. Aeschbach-Hertig, W.; Gleeson, T. Regional strategies for the accelerating global problem of groundwater depletion. *Nat. Geosci.* **2012**, *5*, 853–861. [[CrossRef](#)]
2. Kang, G. Influence and Control Strategy for Local Settlement for High-Speed Railway Infrastructure. *Engineering* **2016**, *2*, 374–379. [[CrossRef](#)]
3. Liu, J.; Yao, H.-l.; Hu, M.-l.; Lu, Z.; Yu, D.-m.; Chen, F.-g. Study of moisture dynamic response and underground drainage test of subgrade model under water level fluctuation. *Rock Soil Mech.* **2012**, *33*, 2917–2922.
4. Wu, B. Three-dimensional seepage-stress coupling analysis of bridge foundation behaviors induced by precipitation. *Chin. J. Rock Mech. Eng.* **2009**, *28*, 3277–3281.
5. Xia, L.-n.; Miao, Y.-d.; LIAO, C.-b. Three-dimensional numerical simulation of influences of ground subsidence on composite foundation. *Rock Soil Mech.* **2012**, *33*, 1217–1222.
6. Feng, W.; Shum, C.; Zhong, M.; Pan, Y. Groundwater storage changes in China from satellite gravity: An overview. *Remote Sens.* **2018**, *10*, 674. [[CrossRef](#)]
7. Rodell, M.; Houser, P.; Jambor, U.; Gottschalck, J.; Mitchell, K.; Meng, C.-J.; Arsenault, K.; Cosgrove, B.; Radakovich, J.; Bosilovich, M. The global land data assimilation system. *Bull. Am. Meteorol. Soc.* **2004**, *85*, 381–394. [[CrossRef](#)]
8. Chen, F.; Mitchell, K.; Schaake, J.; Xue, Y.; Pan, H.L.; Koren, V.; Duan, Q.Y.; Ek, M.; Betts, A. Modeling of land surface evaporation by four schemes and comparison with FIFE observations. *J. Geophys. Res. Atmos.* **1996**, *101*, 7251–7268. [[CrossRef](#)]
9. Koster, R.D.; Suarez, M.J. Modeling the land surface boundary in climate models as a composite of independent vegetation stands. *J. Geophys. Res. Atmos.* **1992**, *97*, 2697–2715. [[CrossRef](#)]
10. Liang, X.; Lettenmaier, D.P.; Wood, E.F.; Burges, S.J. A simple hydrologically based model of land surface water and energy fluxes for general circulation models. *J. Geophys. Res. Atmos.* **1994**, *99*, 14415–14428. [[CrossRef](#)]
11. Lawrence, D.M.; Oleson, K.W.; Flanner, M.G.; Thornton, P.E.; Swenson, S.C.; Lawrence, P.J.; Zeng, X.; Yang, Z.-L.; Levis, S.; Sakaguchi, K.; et al. Parameterization improvements and functional and structural advances in Version 4 of the Community Land Model. *J. Adv. Model. Earth Syst.* **2011**, *3*. [[CrossRef](#)]
12. Clark, D.B.; Mercado, L.M.; Sitch, S.; Jones, C.D.; Gedney, N.; Best, M.J.; Pryor, M.; Rooney, G.G.; Essery, R.L.H.; Blyth, E.; et al. The Joint UK Land Environment Simulator (JULES), model description—Part 2: Carbon fluxes and vegetation dynamics. *Geosci. Model Dev.* **2011**, *4*, 701–722. [[CrossRef](#)]
13. Alcamo, J.; Döll, P.; Kaspar, F.; Siebert, S. *Global Change and Global Scenarios of Water Use and Availability: An Application of WaterGAP 1.0*; Center for Environmental Systems Research: Kassel, Germany, 1997.
14. Vörösmarty, C.J.; Federer, C.A.; Schloss, A.L. Potential evaporation functions compared on US watersheds: Possible implications for global-scale water balance and terrestrial ecosystem modeling. *J. Hydrol.* **1998**, *207*, 147–169. [[CrossRef](#)]
15. Van Beek, L.P.H.; Bierkens, M.F.P. *The Global Hydrological Model PCR-GLOBWB: Conceptualization, Parameterization and Verification*; Report Department of Physical Geography, Utrecht University : Utrecht, The Netherlands, 2009; Available online: <http://vanbeek.geo.uu.nl/suppinfo/vanbeekbierkens2009.pdf>.

16. Bierkens, M.F.P. Global hydrology 2015: State, trends, and directions. *Water Resour. Res.* **2015**, *51*, 4923–4947. [[CrossRef](#)]
17. Döll, P.; Müller Schmied, H.; Schuh, C.; Portmann, F.T.; Eicker, A. Global-scale assessment of groundwater depletion and related groundwater abstractions: Combining hydrological modeling with information from well observations and GRACE satellites. *Water Resour. Res.* **2014**, *50*, 5698–5720. [[CrossRef](#)]
18. Rodell, M.; Velicogna, I.; Famiglietti, J.S. Satellite-based estimates of groundwater depletion in India. *Nature* **2009**, *460*, 999. [[CrossRef](#)]
19. Güntner, A. Improvement of global hydrological models using GRACE data. *Surv. Geophys.* **2008**, *29*, 375–397. [[CrossRef](#)]
20. Landerer, F.W.; Swenson, S. Accuracy of scaled GRACE terrestrial water storage estimates. *Water Resour. Res.* **2012**, *48*, 4531. [[CrossRef](#)]
21. Swenson, S.; Wahr, J. Post-processing removal of correlated errors in GRACE data. *Geophys. Res. Lett.* **2006**, *33*. [[CrossRef](#)]
22. Watkins, M.M.; Wiese, D.N.; Yuan, D.-N.; Boening, C.; Landerer, F.W. Improved methods for observing Earth's time variable mass distribution with GRACE using spherical cap mascons. *J. Geophys. Res. Solid Earth* **2015**, *120*, 2648–2671. [[CrossRef](#)]
23. Wiese, D.N.; Landerer, F.W.; Watkins, M.M. Quantifying and reducing leakage errors in the JPL RL05M GRACE mascon solution. *Water Resour. Res.* **2016**, *52*, 7490–7502. [[CrossRef](#)]
24. Save, H.; Bettadpur, S.; Tapley, B.D. High-resolution CSR GRACE RL05 mascons. *J. Geophys. Res. Solid Earth* **2016**, *121*, 7547–7569. [[CrossRef](#)]
25. Huang, Z.; Pan, Y.; Gong, H.; Yeh, P.J.F.; Li, X.; Zhou, D.; Zhao, W. Subregional-scale groundwater depletion detected by GRACE for both shallow and deep aquifers in North China Plain. *Geophys. Res. Lett.* **2015**, *42*, 1791–1799. [[CrossRef](#)]
26. Feng, W.; Zhong, M.; Lemoine, J.M.; Biancale, R.; Hsu, H.T.; Xia, J. Evaluation of groundwater depletion in North China using the Gravity Recovery and Climate Experiment (GRACE) data and ground-based measurements. *Water Resour. Res.* **2013**, *49*, 2110–2118. [[CrossRef](#)]
27. Wang, X.; de Linage, C.; Famiglietti, J.; Zender, C.S. Gravity Recovery and Climate Experiment (GRACE) detection of water storage changes in the Three Gorges Reservoir of China and comparison with *in situ* measurements. *Water Resour. Res.* **2011**, *47*. [[CrossRef](#)]
28. Zhong, Y.; Zhong, M.; Feng, W.; Zhang, Z.; Shen, Y.; Wu, D. Groundwater depletion in the West Liaohe River Basin, China and its Implications revealed by GRACE and *in situ* measurements. *Remote Sens.* **2018**, *10*, 493. [[CrossRef](#)]
29. Shen, H.; Leblanc, M.; Tweed, S.; Liu, W. Groundwater depletion in the Hai River Basin, China, from *in situ* and GRACE observations. *Hydrol. Sci. J.* **2015**, *60*, 671–687. [[CrossRef](#)]
30. Shamsudduha, M.; Taylor, R.; Longuevergne, L. Monitoring groundwater storage changes in the highly seasonal humid tropics: Validation of GRACE measurements in the Bengal Basin. *Water Resour. Res.* **2012**, *48*. [[CrossRef](#)]
31. Earth2Observe. Global Earth Observation for Integrated Water Resource Assessment. Available online: <http://www.earth2observe.eu/> (accessed on 1 January 2018).
32. Döll, P.; Kaspar, F.; Lehner, B. A global hydrological model for deriving water availability indicators: model tuning and validation. *J. Hydrol.* **2003**, *270*, 105–134. [[CrossRef](#)]
33. China Institute of Geological Environment Monitoring (CIGEM). *China Geological Environment Monitoring: Groundwater Yearbook*; China Land Press: Beijing, China, 2013.
34. Huffman, G.J.; Bolvin, D.T.; Nelkin, E.J.; Wolff, D.B.; Adler, R.F.; Gu, G.; Hong, Y.; Bowman, K.P.; Stocker, E.F. The TRMM multisatellite precipitation analysis (TMPA): Quasi-global, multiyear, combined-sensor precipitation estimates at fine scales. *J. Hydrometeorol.* **2007**, *8*, 38–55. [[CrossRef](#)]
35. Voss, K.A.; Famiglietti, J.S.; Lo, M.; de Linage, C.; Rodell, M.; Swenson, S.C. Groundwater depletion in the Middle East from GRACE with implications for transboundary water management in the Tigris-Euphrates-Western Iran region. *Water Resour. Res.* **2013**, *49*, 904–914. [[CrossRef](#)] [[PubMed](#)]
36. Long, D.; Chen, X.; Scanlon, B.R.; Wada, Y.; Hong, Y.; Singh, V.P.; Chen, Y.; Wang, C.; Han, Z.; Yang, W. Have GRACE satellites overestimated groundwater depletion in the Northwest India Aquifer? *Sci. Rep.* **2016**, *6*, 24398. [[CrossRef](#)] [[PubMed](#)]

37. Theil, H. A rank-invariant method of linear and polynomial regression analysis. In *Henri Theil's Contributions to Economics and Econometrics*; Raj, B., Koerts, J., Eds.; Springer: Berlin, Germany, 1992; pp. 345–381.
38. Hoaglin, D.C.; Mosteller, F.; Tukey, J.W. *Understanding Robust and Exploratory Data Analysis*; Wiley: Hoboken, NJ, USA, 2000.
39. Mann, H.B. Nonparametric tests against trend. *Econ. J. Econom. Soc.* **1945**, 245–259. [[CrossRef](#)]
40. Kendall, M.G. *Rank Correlation Methods*; Griffin: Oxford, England, 1948; Available online: <https://psycnet.apa.org/record/1948-15040-000>.
41. Gilbert, R.O. *Statistical Methods for Environmental Pollution Monitoring*; John Wiley & Sons: Hoboken, NJ, USA, 1987.
42. Asoka, A.; Gleeson, T.; Wada, Y.; Mishra, V. Relative contribution of monsoon precipitation and pumping to changes in groundwater storage in India. *Nat. Geosci.* **2017**, *10*, 109–117. [[CrossRef](#)]
43. Lorenz, E.N. Empirical orthogonal functions and statistical weather prediction. *Open J. Stat.* **1956**, *3*, 1–52.
44. Schmidt, R.; Petrovic, S.; Güntner, A.; Barthelmes, F.; Wunsch, J.; Kusche, J. Periodic components of water storage changes from GRACE and global hydrology models. *J. Geophys. Res. Solid Earth* **2008**, *113*. [[CrossRef](#)]
45. Smith, T.M.; Reynolds, R.W.; Livezey, R.E.; Stokes, D.C. Reconstruction of historical sea surface temperatures using empirical orthogonal functions. *J. Clim.* **1996**, *9*, 1403–1420. [[CrossRef](#)]
46. Arneborg, L.; Wåhlin, A.; Björk, G.; Liljebladh, B.; Orsi, A. Persistent inflow of warm water onto the central Amundsen shelf. *Nat. Geosci.* **2012**, *5*, 876. [[CrossRef](#)]
47. Long, D.; Pan, Y.; Zhou, J.; Chen, Y.; Hou, X.; Hong, Y.; Scanlon, B.R.; Longuevergne, L. Global analysis of spatiotemporal variability in merged total water storage changes using multiple GRACE products and global hydrological models. *Remote Sens. Environ.* **2017**, *192*, 198–216. [[CrossRef](#)]
48. Preisendorfer, R.W.; Mobley, C.D.; Barnett, T.P. The principal discriminant method of prediction: Theory and evaluation. *J. Geophys. Res. Atmos.* **1988**, *93*, 10815–10830. [[CrossRef](#)]
49. Ferreira, V.G.; Montecino, H.D.; Yakubu, C.I.; Heck, B. Uncertainties of the Gravity Recovery and Climate Experiment time-variable gravity-field solutions based on three-cornered hat method. *J. Appl. Remote Sens.* **2016**, *10*, 015015. [[CrossRef](#)]
50. Awange, J.; Ferreira, V.; Forootan, E.; Andam-Akorful, S.; Agutu, N.; He, X. Uncertainties in remotely sensed precipitation data over Africa. *Int. J. Climatol.* **2016**, *36*, 303–323. [[CrossRef](#)]
51. Torcaso, F.; Ekstrom, C.; Burt, E.; Matsakis, D. *Estimating Frequency Stability and Cross-Correlations*; Naval Observatory: Washington, DC, USA, 1998.
52. Galindo, F.J.; Palacio, J. *Estimating the Instabilities of N Correlated Clocks*; Real Observatorio de la Armada (SPAIN): Cádiz, Spain, 1999.
53. Chin, T.; Gross, R.; Dickey, J. Multi-reference evaluation of uncertainty in Earth orientation parameter measurements. *J. Geod.* **2005**, *79*, 24–32. [[CrossRef](#)]
54. Koot, L.; De Viron, O.; Dehant, V. Atmospheric angular momentum time-series: characterization of their internal noise and creation of a combined series. *J. Geod.* **2006**, *79*, 663. [[CrossRef](#)]
55. Galindo, F.J.; Palacio, J. Post-processing ROA data clocks for optimal stability in the ensemble timescale. *Metrologia* **2003**, *40*, S237. [[CrossRef](#)]
56. Xiang, L.; Wang, H.; Steffen, H.; Wu, P.; Jia, L.; Jiang, L.; Shen, Q. Groundwater storage changes in the Tibetan Plateau and adjacent areas revealed from GRACE satellite gravity data. *Earth Planet. Sci. Lett.* **2016**, *449*, 228–239. [[CrossRef](#)]
57. Farinotti, D.; Longuevergne, L.; Moholdt, G.; Duethmann, D.; Mölg, T.; Bolch, T.; Vorogushyn, S.; Güntner, A. Substantial glacier mass loss in the Tien Shan over the past 50 years. *Nat. Geosci.* **2015**, *8*, 716. [[CrossRef](#)]
58. Yi, S.; Wang, Q.; Chang, L.; Sun, W. Changes in mountain glaciers, lake levels, and snow coverage in the Tianshan monitored by GRACE, ICESat, altimetry, and MODIS. *Remote Sens.* **2016**, *8*, 798. [[CrossRef](#)]
59. Jacob, T.; Wahr, J.; Pfeffer, W.T.; Swenson, S. Recent contributions of glaciers and ice caps to sea level rise. *Nature* **2012**, *482*, 514. [[CrossRef](#)]
60. Gardner, A.S.; Moholdt, G.; Cogley, J.G.; Wouters, B.; Arendt, A.A.; Wahr, J.; Berthier, E.; Hock, R.; Pfeffer, W.T.; Kaser, G. A reconciled estimate of glacier contributions to sea level rise: 2003 to 2009. *Science* **2013**, *340*, 852–857. [[CrossRef](#)] [[PubMed](#)]
61. Rodell, M.; Famiglietti, J.; Wiese, D.; Reager, J.; Beaulieu, H.; Landerer, F.W.; Lo, M.-H. Emerging trends in global freshwater availability. *Nature* **2018**, *557*, 651. [[CrossRef](#)] [[PubMed](#)]

62. Changming, L.; Jingjie, Y.; Kendy, E. Groundwater exploitation and its impact on the environment in the North China Plain. *Water Int.* **2001**, *26*, 265–272. [[CrossRef](#)]
63. Yang, X.; Chen, Y.; Pacenka, S.; Gao, W.; Zhang, M.; Sui, P.; Steenhuis, T.S. Recharge and groundwater use in the North China Plain for six irrigated crops for an eleven year period. *PLoS ONE* **2015**, *10*, e0115269. [[CrossRef](#)] [[PubMed](#)]
64. Geographic Data Sharing Infrastructure. College of Urban and Environmental Science, Peking University. Available online: <http://geodata.pku.edu.cn> (accessed on 10 December 2019).
65. Li, B.; Rodell, M.; Kumar, S.; Beaudoin, H.K.; Getirana, A.; Zaitchik, B.F.; de Goncalves, L.G.; Cossetin, C.; Bhanja, S.; Mukherjee, A. Global GRACE data assimilation for groundwater and drought monitoring: advances and challenges. *Water Resour. Res.* **2019**, *55*, 7564–7586. [[CrossRef](#)]
66. Tangdamrongsub, N.; Steele-Dunne, S.; Gunter, B.; Ditmar, P.; Weerts, A. Data assimilation of GRACE terrestrial water storage estimates into a regional hydrological model of the Rhine River basin. *Hydrol. Earth Syst. Sci.* **2015**, *19*. [[CrossRef](#)]
67. Tangdamrongsub, N.; Han, S.-C.; Tian, S.; Müller Schmied, H.; Sutanudjaja, E.H.; Ran, J.; Feng, W. Evaluation of groundwater storage variations estimated from GRACE data assimilation and state-of-the-art land surface models in Australia and the North China Plain. *Remote Sens.* **2018**, *10*, 483. [[CrossRef](#)]
68. Eicker, A.; Schumacher, M.; Kusche, J.; Döll, P.; Schmied, H.M. Calibration/data assimilation approach for integrating GRACE data into the WaterGAP Global Hydrology Model (WGHM) using an ensemble Kalman filter: First results. *Surv. Geophys.* **2014**, *35*, 1285–1309. [[CrossRef](#)]
69. Giroto, M.; De Lannoy, G.J.; Reichle, R.H.; Rodell, M.; Draper, C.; Bhanja, S.N.; Mukherjee, A. Benefits and pitfalls of GRACE data assimilation: A case study of terrestrial water storage depletion in India. *Geophys. Res. Lett.* **2017**, *44*, 4107–4115. [[CrossRef](#)]



© 2020 by the authors. Licensee MDPI, Basel, Switzerland. This article is an open access article distributed under the terms and conditions of the Creative Commons Attribution (CC BY) license (<http://creativecommons.org/licenses/by/4.0/>).